Astronomy & Astrophysics manuscript no. output
May 29, 2026
©ESO 2026

Chromospheric condensation and heating in small-scale flaring events: Insights from GREGOR/GRIS and coordinated IRIS observations

F. Ferrente[1]⋆, S. L. Guglielmino[1], P. Romano[1], D. Spadaro[1], M. Murabito[2], L. Contarino[1], V. Andretta[3], I. Ermolli[2], S. J. González Manrique[4,5], C. Kuckein[4,5], C. Sasso[3], and S. M. Lezzi[6]

[1] INAF – Osservatorio Astrofisico di Catania, Via S. Sofia 78, 95123 Catania, Italy
e-mail: fabiana.ferrente@inaf.it
[2] INAF – Osservatorio Astronomico di Roma, Via Frascati 33, 00078 Monte Porzio Catone, Italy
[3] INAF – Osservatorio Astronomico di Capodimonte, Salita Moiariello 16, 80131 Napoli, Italy
[4] Instituto de Astrofísica de Canarias, Vía Láctea s/n, 38205 La Laguna, Tenerife, Spain
[5] Departamento de Astrofísica, Universidad de La Laguna, 38205, La Laguna, Tenerife, Spain
[6] INAF - Capodimonte Astronomical Observatory, Salita Moiariello 16, I 80131 Napoli, Italy; now at CMCC Foundation - Euro-Mediterranean Center on Climate Change, Italy

Received – ; accepted –

ABSTRACT

We present a detailed analysis of the chromospheric response during a small-scale flaring event observed in the active region NOAA 13394 on 8 August 2023. By utilizing coordinated high-resolution spatial and spectral observations from the GRIS spectropolarimeter at the GREGOR telescope, targeting the He I 1083.0 nm triplet, and the IRIS spectrograph, covering the near- and far-ultraviolet spectral regions, we investigate the plasma dynamics and heating processes within the solar atmosphere. We observe complex, asymmetric He I Stokes profiles; inversions performed with the state-of-the-art HAZEL code reveal that these profiles are characterized by significant redshifts, with velocities reaching $\sim$ 30 km s^{-1}, which are interpreted as signatures of chromospheric condensation. These findings are supported by simultaneous IRIS observations, which show redshifts in transition region lines (Si IV, C II) along the footpoints of the flaring event, suggesting a coherent, multi-layer response to the heating. The evolution of the Mg II h&k line profiles, transitioning from a central reversal to a single-peaked morphology, suggests a rising source function associated with reduced opacity. These features provide compelling evidence of deep heating in the lower chromosphere during the flaring event.

Key words. Sun: magnetic fields – Magnetohydrodynamics (MHD) – Techniques: polarimetric – Radiative transfer – Techniques: high angular resolution

1. Introduction

The He I 1083.0 nm triplet is a well-established diagnostic of the upper chromosphere, highly sensitive to both photoionization by coronal extreme ultraviolet (EUV) photons and direct collisional excitation, particularly during flares. Due to its metastable lower level, the triplet becomes strongly responsive to rapid changes in the impinging radiation field and local thermodynamic conditions (Andretta & Jones 1997; Centeno et al. 2008). In large flares, the He I 1083.0 nm triplet can appear in emission, while in weaker events or during the early phases of a flare it often manifests with enhanced absorption or broadened profiles. Earlier studies found that the intensity of this triplet is poorly correlated with Hα intensity, but shows a stronger correlation with soft X-ray flux. In particular, excess emission in the 1083.0 nm triplet appears only when the GOES X-ray flux exceeds a certain threshold, generally above that of mid C-class flares (You & Oertel 1992; Penn & Kuhn 1995; Li et al. 2007; Du & Li 2008; Zeng et al. 2014). Regarding the formation of the helium spectrum and observations of the He I 1083.0 nm line specifically in C-class flares, relevant studies have been presented by Mauas et al. (2005) and Andretta et al. (2008). High-resolution observations during flares have revealed that this triplet frequently exhibits strong asymmetries and large Doppler shifts, which are interpreted as signatures of chromospheric condensation and evaporation (You & Oertel 1992; Kuckein et al. 2025).

Several spectropolarimetric studies of the He I 1083.0 nm line have shown that complex, asymmetric, or broadened profiles often require multi-component modeling to account for overlapping atmospheric layers with distinct velocities. The necessity of employing multi-component atmospheres to correctly interpret complex chromospheric profiles was first demonstrated by Schmidt et al. (2000). Building on this foundational work, Aznar Cuadrado et al. (2005, 2007) further revealed the presence of multi-component structures in both active and quiet-Sun areas. In the specific context of solar flares, Sasso et al. (2011, 2014) analyzed a C2.0-class event in active region NOAA 9451 and found strong evidence for multiple unresolved components within a single resolution element, revealing simultaneous upflows up to 40 km s^{-1} and downflows reaching 100 km s^{-1}. Such stratified flows and complex velocity structures are indeed ubiquitous. To address these complexities, multi-component inversions have proven to be a valuable tool for modeling complex spectral signatures and characterizing the kinematics in various highly dynamic chromospheric phenomena. These in-

⋆ Corresponding author

Article published by EDP Sciences, to be cited as https://doi.org/10.1051/0004-6361/202659741

clude emerging flux regions, where both Lagg et al. (2007) and González Manrique et al. (2016) found similar signatures such as dual or multi-peak He I absorption profiles, as well as arch filament systems (González Manrique et al. 2018) and erupting filaments (Kuckein et al. 2020).

These stratified flows and unresolved substructures are often signatures of the underlying complex coupling between energy release and plasma response. A particularly prominent manifestation of this coupling is the generation of bidirectional mass motions, known as chromospheric evaporation and condensation. Pioneering soft X-ray observations of the Ca XIX and Fe XXV lines by Antonucci (1982); Antonucci et al. (1984) provided the first clear evidence of the evaporative component, characterized by blue-shifted profiles indicative of upflowing plasma. Inextricably linked to this upward expansion is the chromospheric condensation, where momentum balance requirements drive a downward compression of the cooler, denser plasma. Hydrodynamic models assuming transient heating localized at the loop footpoints have successfully reproduced the significant redshifts observed in transition region lines (Spadaro et al. 2006). Modern UV studies, using lines such as Mg II h&k (2796 and 2804 Å), C II (1335 Å), and Si IV (1400 Å) (Tian et al. 2014, 2015; Li et al. 2017; Graham & Cauzzi 2015; Polito et al. 2016; Tei et al. 2018), consistently report strong downflows with velocities ranging from 10 to 80 km s^{-1} during the impulsive phase of solar flares. These downflows are the direct observational signature of the chromospheric condensation following the rapid energy deposition.

Chromospheric condensation events have also been investigated through spectropolarimetric analyses. Kuridze et al. (2017) reported that the flaring chromosphere was dominated by weak downflowing condensations at the formation height of the Ca II 854.2 nm line during a C-class flare. Libbrecht et al. (2019) detected strong redshifts of about 60 km s^{-1} in the He I D_3 line at 587.6 nm during a similar-class event. Their observations suggest that such downflows may shock the deeper chromosphere, producing broad and modestly blueshifted D_3 profiles interpreted as secondary upflows. In a multi-line spectropolarimetric study of a C-class flare, Yadav et al. (2021) found a downflow of 12 km s^{-1} at the flare footpoint in the lower atmosphere ($\log\tau = -2.5$ to -3.5), accompanied by simultaneous upflows in higher layers ($\log\tau = -3.5$ to -5.5), which they interpreted as chromospheric condensation in the lower layers and evaporation in the upper regions. More recently, Kuckein et al. (2025) analyzed an M-class flare using both the He I 1083.0 nm and Ca II 854.2 nm infrared lines. They reported redshifts of 2 to 13 km s^{-1} in He I 1083.0 nm at the flare kernels, along with the appearance of post-flare loop-like structures. These loops showed strong footpoint downflows in He I 1083.0 nm, reaching up to $\approx$ 40 km s^{-1}, while associated downflows in Ca II 854.2 nm remained more moderate, around 10 km s^{-1}.

In this work, we present high-resolution observations of the chromospheric response in the He I triplet to a localized brightening, obtained with the GREGOR telescope (Schmidt et al. 2012; Kleint et al. 2020) on 8 August 2023. The event was initially identified in context imaging from the High-resolution Fast Imager (HiFI+; Denker et al. 2023) installed at the GREGOR telescope, and in Interface Region Imaging Spectrograph (IRIS; De Pontieu et al. 2014) slit-jaw observations, while the chromospheric response was analyzed through spectropolarimetric data from the GREGOR Infrared Spectrograph (GRIS; Collados et al. 2012) instrument and IRIS spectroscopic measurements.

2. Observations

The active region (AR) NOAA 13394 (hereafter AR13394) emerged on the eastern limb of the Sun on 2 August 2023. By August 8, it had progressed to a position at S23W03 (45″, −464″) and exhibited a sunspot area of 140 millionths of the solar disk. AR13394 was a compact group with a single symmetric dominant spot and was classified as Cso according to the McIntosh classification system (see Fig. 1 third panel). During its transit across the solar disk, AR13394 produced only C-class and weaker flares.

Figure 1 shows a full-disk line-of-sight (LOS) magnetogram of the Sun, obtained by the Helioseismic and Magnetic Imager (HMI; Scherrer et al. 2012) onboard on the Solar Dynamics Observatory (SDO; Pesnell et al. 2012), along with a zoomed-in view of AR13394.

The zoomed-in view reveals the structure of AR13394, with its main sunspot exhibiting a strong negative polarity; surrounding the sunspot, especially to the East and South patches of positive polarity are visible, indicating a complex magnetic configuration.

We also used data from the Atmospheric Imaging Assembly (AIA; Lemen et al. 2012) onboard SDO. AIA provided full-disk EUV images of the solar corona and transition region. For this study, we specifically used the 304 Å (He II, T ~0.05 MK), 171 Å (Fe IX, T ~0.7 MK), 94 Å (Fe XVIII, T ~6.3 MK), and 131 Å (Fe VIII, XXI, T ~0.4 MK and ~10 MK) passbands to analyze the context and multi-thermal evolution of the brightening event.

We observed AR13394 during a coordinated campaign conducted from 7 to 9 August 2023, supported by the SOLARNET project[1], using the GREGOR telescope and the IRIS satellite (De Pontieu et al. 2014). On 8 August 2023, a single successful spectropolarimetric raster scan was acquired with GRIS between 09:18 UT and 09:32 UT. The scan was centered on a small Hα brightening in the eastern penumbra of the main sunspot. A second scan, attempted at 09:33 UT, was immediately aborted due to a rapid deterioration of the seeing conditions. The successful scan was performed with the slit oriented at 0° (parallel to the solar equator) and consisted of 100 steps with a step size of 0.″135. Given the exposure time of 250 ms and six accumulations per position, the scan covered a total FOV of 13.″5 × 60″ (see the rectangles in Fig. 2).

During the scan, GRIS recorded full-Stokes spectra within a 1.8 nm-wide spectral window including the He I 1083.0 nm triplet, the photospheric Si I 1082.7 nm, and the Ca I 1083.9 nm lines. Simultaneously, near-infrared slit-jaw images at 900 nm and high-resolution context images with HiFI+ were recorded. HiFI+ No. 1 captured the G-band (430.7 nm) and blue continuum (450.6 nm) at a 12-second cadence (FOV 70.″7 × 59.″6), while HiFI+ No. 2 observed Hα (656.3 nm) in both narrowband and broadband at a 6-second cadence (FOV 76.″5 × 60.″5). HiFI+ No. 3 acquired Ca II H (396.8 nm) and TiO (705.7 nm) also at a 6-second cadence.

The GRIS data were reduced using the standard pipeline (Collados 1999, 2003), which performs dark-current subtraction, flat-field correction, polarimetric calibration, and instrumental cross-talk removal. The HiFI+ data were processed with the sTools pipeline (Kuckein et al. 2017).

The IRIS satellite performed coordinated observations consisting of raster scans and slit-jaw images (SJIs). The raster scan covered a FOV of 5″ × 119″ using 16 steps of 0.″35 with a step cadence of 16.1 s. This resulted in a total of 49 complete rasters,

[1] https://www.solarnet-project.eu/

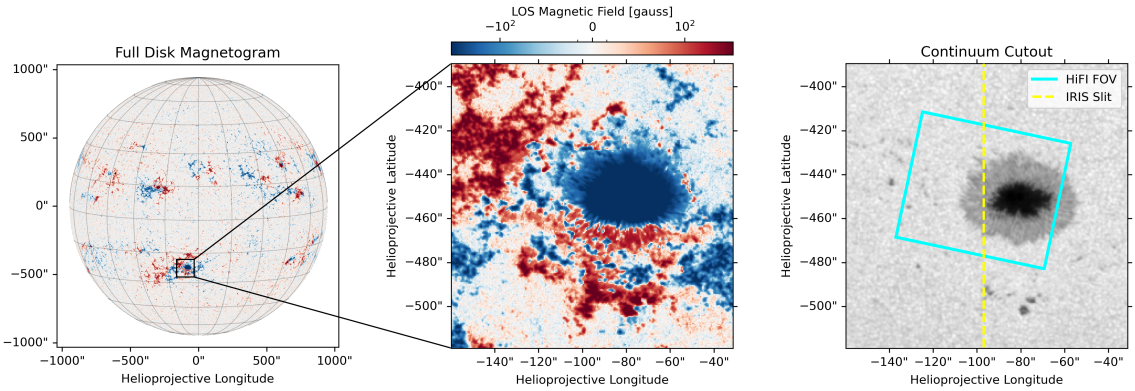


Fig. 1. SDO/HMI observations of AR 13394 on 8 August 2023. The left panel shows the full-disk longitudinal magnetogram at 09:17 UT, where red and blue represent positive and negative polarities, respectively. The black rectangular box highlights the region of interest, corresponding to the IRIS FOV, magnified in the center panel, with the color bar quantifying the LOS magnetic field strength in gauss. The right panel displays the corresponding HMI continuum image at 617.3 nm captured at 09:16 UT. The solid cyan box outlines the exact FOV of the GREGOR/HiFI+ instrument, encompassing the main sunspot and the dashed yellow line indicates the position of the IRIS slit.

with a full raster cadence of 258 s. Simultaneously, SJIs provided context imaging in four passbands (1330 Å, 1400 Å, 2796 Å, and 2832 Å) over a larger 120″ × 119″ FOV. The cadence for each filter was approximately 65 s, producing 196 images for the 1330, 1400, and 2796 Å passbands, and 195 images for the 2832 Å passband. The IRIS data used in this work were obtained as Level 2 calibrated files from the LMSAL archive. These products consist of science-ready spectral rasters and slit-jaw image time series that have been processed at LMSAL from Level 1.5 data. The calibration procedure is described by De Pontieu et al. (2014). A summary of the observational settings is provided in Table 1.

3. Overview of the brightening

We monitored AR13394 from 7 to 9 August 2023. In this work, we focus on a brightening event that occurred on 8 August 2023, first detected in the narrowband Hα images of the HiFI+ No. 2 camera. During the acquisition sequence, a GRIS scan was being performed, and all HiFI+ cameras were operating simultaneously.

The G-band images were restored using sets of 100 frames with the speckle restoration code `KISIP` (Wöger & von der Lühe 2008). In addition, HiFI+ recorded pairs of images of the target, one sampling the Hα line core and the other the nearby continuum. The data were acquired in bursts of 500 images. The Hα and continuum image pairs were subsequently used for image restoration employing the Multi-Object Multi-Frame Blind Deconvolution technique (MOMFBD; Van Noort et al. 2005). For each burst, the best 100 frames were selected to produce a single restored image.

Figure 2 presents two of the restored HiFI+ images acquired on 8 August at 09:18 UT. The upper panel displays the blue continuum at 450.6 nm, revealing photospheric structures, while the lower panel shows the narrowband Hα image, highlighting chromospheric features.

The Hα image clearly reveals a brightening within the GRIS field of view (indicated by the blue box in Fig. 2). This feature is located in the eastern part of the sunspot penumbra and extends across the upper–eastern region of the scanned area. The enhanced intensity occupies the region where a dark flux bundle is observed at chromospheric levels, likely corresponding to an arch filament system. The photospheric footpoints of the threads of this bundle are spatially coincident with the little pores seen in the 450.6 nm continuum.

An inspection of the GOES 1–8 Å X-ray flux shows a peak at ~09:16:40 UT, while as reported by the Heliophysics Events Knowledgebase (HEK, SOL2023-08-08T09:15:08) this event was automatically identified in the catalog using AIA 131 Å filtergrams, with a recorded peak time at 09:17:08 UT. The event reached a peak flux of 2.5×10^{-6} W m^{-2}, classifying it as a C-class flare (see Fig. 3).

We include the normalized light curves of the AIA 131 Å channel and the HiFI+2 Hα narrowband channel in Fig. 3. It should be noted that while Fig. 2 displays the restored images, the light curve in Fig. 3 was derived from the reduced (non-restored) HiFI+2 data. To compare the chromospheric and coronal responses, the SDO/AIA maps were spatially aligned and cropped to match the full FOV of GREGOR/HiFI+. This ensures that the light curves for both instruments were extracted from the same physical portion of the active region, covering the flare kernels. The mean intensity for each frame was computed by calculating the spatial average of the counts across all pixels within the HiFI+ FOV. The resulting values were subsequently normalized to their respective maximum intensities to facilitate a direct comparison of the temporal evolution across different instruments.

Although the HiFI+2 observations began at 09:18:28 UT, shortly after the main X-ray peak, the light curve reveals a distinct secondary bump around 09:24 UT. This feature is temporally correlated with a similar enhancement found in the AIA 131 Å channel, suggesting a secondary impulsive energy release. Therefore, although our GREGOR observations miss the primary impulsive phase, they still capture the flare during its gradual phase. Note that the soft X-ray background remained elevated throughout the day, indicating an overall highly active solar state.

To provide broader atmospheric context, Fig. 4 presents a multi-channel sequence of EUV images capturing the evolution of the brightening. The sequence was acquired with SDO/AIA in four EUV channels (304 Å, 171 Å, 94 Å, and 131 Å), arranged from left to right in order of increasing characteristic formation temperature. The top row displays a larger FOV for spatial context, where a dashed white box outlines the region of interest, and a solid white rectangle indicates the FOV of the HiFI+ instrument. The subsequent rows illustrate the temporal evolution

Table 1. Summary of the coordinated GRIS, IRIS, and HiFI+ observations.

Instrument	Time (UT)	Observation type	Parameters
GRIS	09:18–09:32	Single raster scan	100 steps of 0.″135
HiFI+1	09:18–09:32	Time sequence; imaging	G-band/Blue cont.; Exp: 1 ms; Frame rate: 49 Hz; Cadence: ∼12 s
HiFI+2	09:18–09:32	Time sequence; imaging	Hα (NB/BB); Exp: 9 ms; Frame rate: 100 Hz; Cadence: ∼6 s
HiFI+3	09:21–09:32	Time sequence; imaging	Ca II H/TiO; Exp: 9/0.4 ms; Frame rate: 100 Hz; Cadence: ∼6 s
IRIS	06:56–10:27	Large dense 16-step raster + Slit-Jaw images	16 steps of 0.″35; step cadence: 16.1 s; Raster cadence: 258 s (49 rasters)

of the area within the dashed box, centered on the brightening event, with an effective cadence of about 1 minute.

The 304 Å passband (first column) captures the chromospheric and transition region response, where brightenings appear near the loop footpoints in the upper-left portion of the sub-FOV starting around 09:15 UT and resembling the shape of the brightening observed by HiFI+ shown in Fig. 2. These brightenings intensify and expand as the event progresses. In the 171 Å channel (second column), the brightening events are less pronounced, yet their morphology and timing remain largely cospatial and consistent with those observed in the 304 Å sequence, indicating a coherent response across multiple atmospheric layers.

The 94 Å and 131 Å channels (third and fourth columns) refer to hotter plasma components, highlighting the formation of high-temperature loops as the event progresses. In these passbands, we see that the loops start to brighten, with clear signatures of hot plasma appearing from 09:17 UT onwards. This temporal progression suggests rapid heating and plasma flows, typically associated with magnetic reconnection processes. A comparison across the different passbands and time frames provides a clear visualization of the spatial and thermal structuring of the solar atmosphere during the brightening. Notably, the initial increase in brightness in the 131 Å passband coincides with the brightening of the footpoints in the lower atmosphere, initially observed in the 304 Å and 171 Å channels. Subsequently, hotter plasma becomes more visible in the 94 Å channel, marking the upward propagation of energy and the heating of coronal loops during the brightening event.

Figure 5 shows the temporal evolution of the brightening event as observed by three different instruments. The left column displays high-resolution HiFI+2 images, the middle column shows AIA 304 Å observations, and the right column presents IRIS SJI 1330 Å maps. To facilitate the comparison between datasets with different spatial resolutions, cyan contours outlining the brightest regions identified in the HiFI+2 images are overplotted on all panels. Their close spatial correspondence indicates a high degree of cospatiality between the brightenings observed at different atmospheric layers. The three rows illustrate the evolution of the event at three nearly co-temporal time steps, enabling a direct comparison of the temporal and spatial evolution observed by the different instruments.

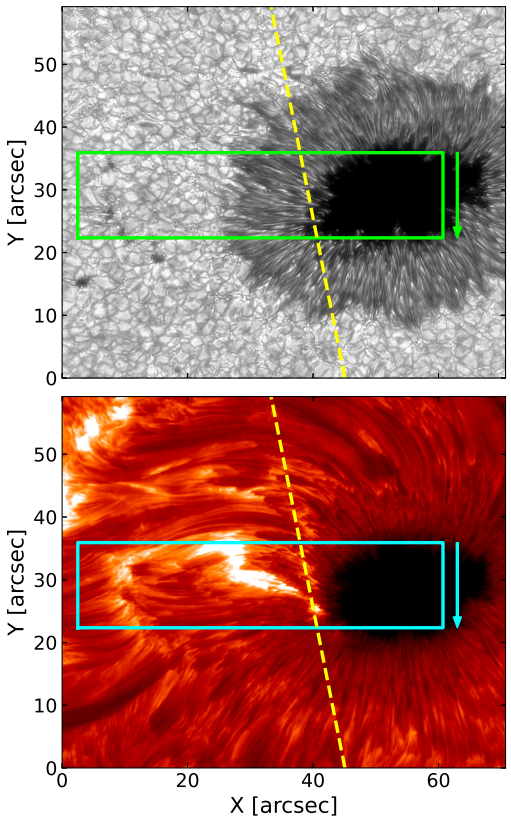


Fig. 2. Restored context images taken by HiFI+ in the blue continuum at 450.6 nm (top panel) and in the Hα line (bottom panel) at 09:18 UT on 8 August. The green and cyan rectangles outline the FOV scanned by the GRIS spectrograph. The dashed yellow line marks the first slit position of the IRIS observations. The arrows indicate the scan direction.

4. Data analysis

4.1. Spectral properties

This section presents the GRIS observations of AR13394 acquired on 8 August 2023. Figure 6 displays the maps of the four Stokes parameters obtained with GRIS for two different spectral lines: the He I 1083.0 nm triplet and the photospheric Si I 1082.7 nm line. The He I triplet is formed by three transitions but due to their proximity, the two transitions at longer wavelengths are typically blended and referred to as the "red" component, while the isolated transition at shorter wavelengths ($\approx$ 1082.9 nm) is known as the "blue" component (see, e.g., Centeno et al. 2008). Note that the FOV shown in Fig. 6 specifically refers to the red component, and has been restricted compared to the full scan area to exclude the final steps of the acquisition, where the observations were compromised by poor seeing conditions.

In both cases, the Stokes parameters are normalized to the continuum intensity I_c. Since the FOV is located within an active region, I_c was carefully estimated by averaging the signal over the most quiescent pixels available. To ensure a standard calibration, we further corrected this value to represent the disk-center continuum level ($\mu = 1$) by applying a correction factor derived from the Harvard-Smithsonian Reference Atmosphere (HSRA; Gingerich et al. 1971) model, accounting for the limb-darkening

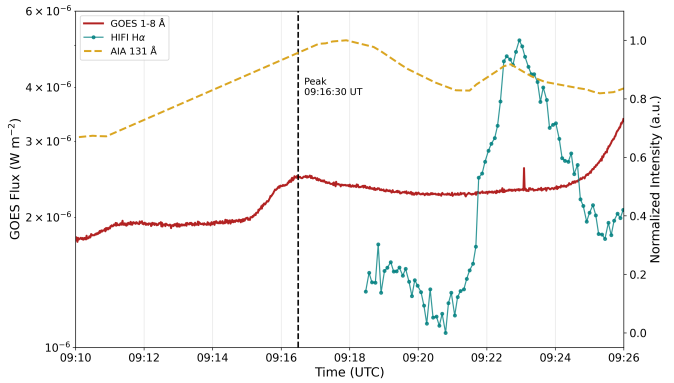


Fig. 3. GOES 1–8 Å X-ray flux (solid red line, left axis, logarithmic scale). The blue (solid with markers) and yellow (dashed) curves show the normalized intensities of the HiFI Hα narrow band and SDO/AIA 131 Å channel, respectively (right axis, arbitrary units).

effect at our specific heliocentric position ($\mu \approx 0.87$). For each line, the top panel shows Stokes I/I_c evaluated at the line core (as indicated for the He I triplet in Fig. 7), while the Q/I_c, U/I_c, and V/I_c maps refer to the blue wing of the line.

For the He I line, the Stokes I/I_c map outlines the morphology of chromospheric structures, with the umbra visible on the right part of the FOV. The left side of the map displays fine, elongated dark structures interspersed with bright features. The signals in the Stokes Q/I_c and U/I_c maps appear considerably noisy. However, weak positive Q/I_c amplitudes and bipolar U/I_c patterns are still recognizable, particularly in the region around $x = 20''$–$40''$. The V/I_c map shows a strong and intricate pattern within the umbra of the main sunspot. The signal appears as alternating regions of enhanced and reduced amplitude, forming a pronounced wavy morphology. This spatially modulated pattern is consistent with the presence of umbral flashes and dynamic chromospheric magnetic field variations (Beckers & Tallant 1969; Felipe et al. 2010).

For the Si I line, the Stokes Q/I_c and U/I_c maps show signals up to about 0.04 in units of the continuum intensity I_c, mainly concentrated in the penumbra. The blue-wing V/I_c map exhibits strong signals across both the umbra and penumbra, with a uniform polarity throughout most of the FOV and a small patch of opposite polarity located around $10'' \times 6''$.

In Figure 7, we show four representative He I 1083.0 nm Stokes I profiles extracted from different locations within the FOV, as indicated in the legend. The solid black profile, marked by a square, corresponds to a relatively quiet profile within the FOV, taken as a reference. The remaining three positions were selected based on distinct spectral features identified in the He I line. In particular, the dotted blue profile (marked by an inverted triangle) shows strong absorption in the red component of the He I triplet (around 1083.03 nm), as well as a clearly defined absorption feature in the blue component at approximately 1082.91 nm. The green dash-dotted profile exhibits broad and strong absorption in a region of enhanced polarization, while the dashed red profile displays an additional absorption feature near 1083.08 nm, absent in the other two. The latter profile is notably broad and exhibits two absorption minima, indicating a superposition of different atmospheric components within the same resolution element. This complex structure suggests that the observed signal samples information from multiple heights or layers in the atmosphere.

4.2. Inversions with HAZEL

In order to retrieve the thermal and magnetic information from the GRIS spectropolarimetric observations, we carried out the inversions of the full FOV using the latest version of the HAZEL code[2] (Asensio Ramos et al. 2008). This updated version allows for the joint inversion of multiple spectral lines, including LTE photospheric lines, chromospheric lines such as the He I triplet using the multi-term approximation, and several telluric lines modeled with the Voigt profile. Moreover, it integrates emergent photospheric intensities computed with the SIR code (Ruiz Cobo & del Toro Iniesta 1992), providing an improved chromospheric model.

To synthesize the Stokes profiles of the He I 1083.0 nm triplet, the HAZEL code uses a constant-property slab model, representing a plasma layer located at a height h above the visible solar surface. In this model, all atoms within the slab, characterized by an optical thickness τ_{slab}, are uniformly illuminated from below by the photospheric continuum radiation (e.g., Yadav et al. 2019). The model parameters include the optical depth at the core of the red component (τ), the damping parameter (a), the Doppler width ($\Delta\lambda_D$), the line-of-sight velocity of the plasma (V_{LOS}), the height of the slab above the solar surface, the heliocentric angle, and the three components of the magnetic field vector. Simultaneously, the code can fit the Stokes profiles of the nearby Si I line, providing complementary information about the photospheric magnetic and velocity fields.

All pixels were inverted using three inversion cycles for both atmospheric layers, i.e., photosphere and chromosphere. The Harvard-Smithsonian reference atmosphere (HSRA; Gingerich et al. 1971) was used as the initial model atmosphere for the Si I spectral line. The inversion code infers the atmospheric parameters by interpolating physical quantities set at specific optical depth points, called nodes. The scheme presented in Table 2 refers specifically to the nodes used for the Si I photospheric inversion. The number of nodes was increased in each successive cycle: two, three, and five nodes were used for temperature; one, two, and three nodes for each component of the magnetic field vector. One node was used for microturbulence and LOS velocity starting from the second cycle (see Table 2). Macroturbulence and filling factor were not inverted and were kept fixed at their initial values of 0.0 km s^{-1} and 1.0, respectively.

Table 2. Number of nodes for the Si I photospheric inversion.

Parameter	Cycle 1	Cycle 2	Cycle 3
Temperature	2	3	5
Bx	1	2	3
By	1	2	3
Bz	1	2	3
LOS velocity	0	1	1
Microturbulence	0	1	1
Macroturbulence	0	0	0
Filling factor	0	0	0

For the He I triplet, the presence of broad and asymmetric profiles motivated the use of a two-slab atmospheric model. However, rather than applying this more complex approach uniformly across the entire FOV, we adopted a hybrid strategy a posteriori. We performed both single-slab and two-slab inversions over the full dataset, and then identified localized regions exhibiting complex profiles based on a line broadening threshold of $\Delta v > 15$ km/s. The final solution was constructed by

[2] https://aasensio.github.io/hazel2

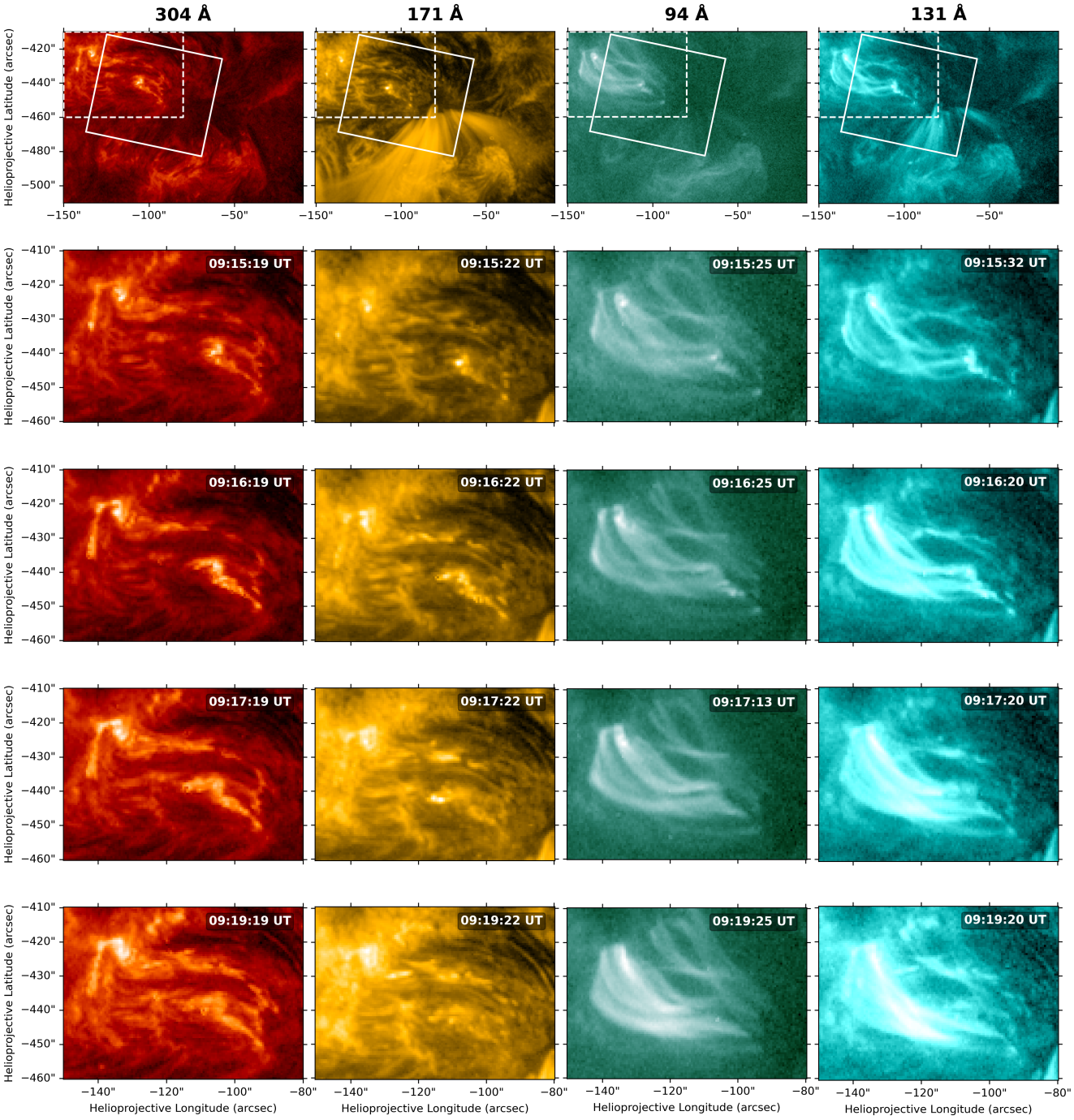


Fig. 4. Multi-wavelength evolution of the active region observed by SDO/AIA. The columns display, from left to right, images in the 304 Å (He II, ~0.05 MK), 171 Å (Fe IX, ~0.7 MK), 94 Å (Fe XVIII, ~6.3 MK), and 131 Å (Fe VIII and Fe XXI, ~0.4 MK and ~10 MK) channels. In each column, the top panel displays a context image with a larger FOV, where the dashed white rectangle outlines the region of interest, chosen to be wide enough to fully encompass the event. The solid white rectangle indicates the FOV of the HiFI+ instrument. The subsequent panels (from top to bottom) show the temporal evolution of this zoomed region (approximate FOV of 70″ × 50″) covering the interval between 09:15 UT and 09:19 UT. The timestamps in each panel indicate the observation time. The sequence reveals the progressive brightening and dynamic morphology of the event at different atmospheric heights.

combining the two results, retaining the single-slab inversions for the majority of the FOV and substituting them with the two-slab configuration only in the selected patches where Δv was larger than the chosen threshold. For the two-slab inversions, we explored different configurations, placing the slabs either at the same height (3.″0) or at different heights, such as 3.″0 and 4.″0, or 3.″0 and 6.″0. Although these geometric heights cannot be directly inferred from disk observations and are therefore treated as representative fixed values, the 3.″0–6.″0 configuration produced more spatially coherent atmospheric parameters and was

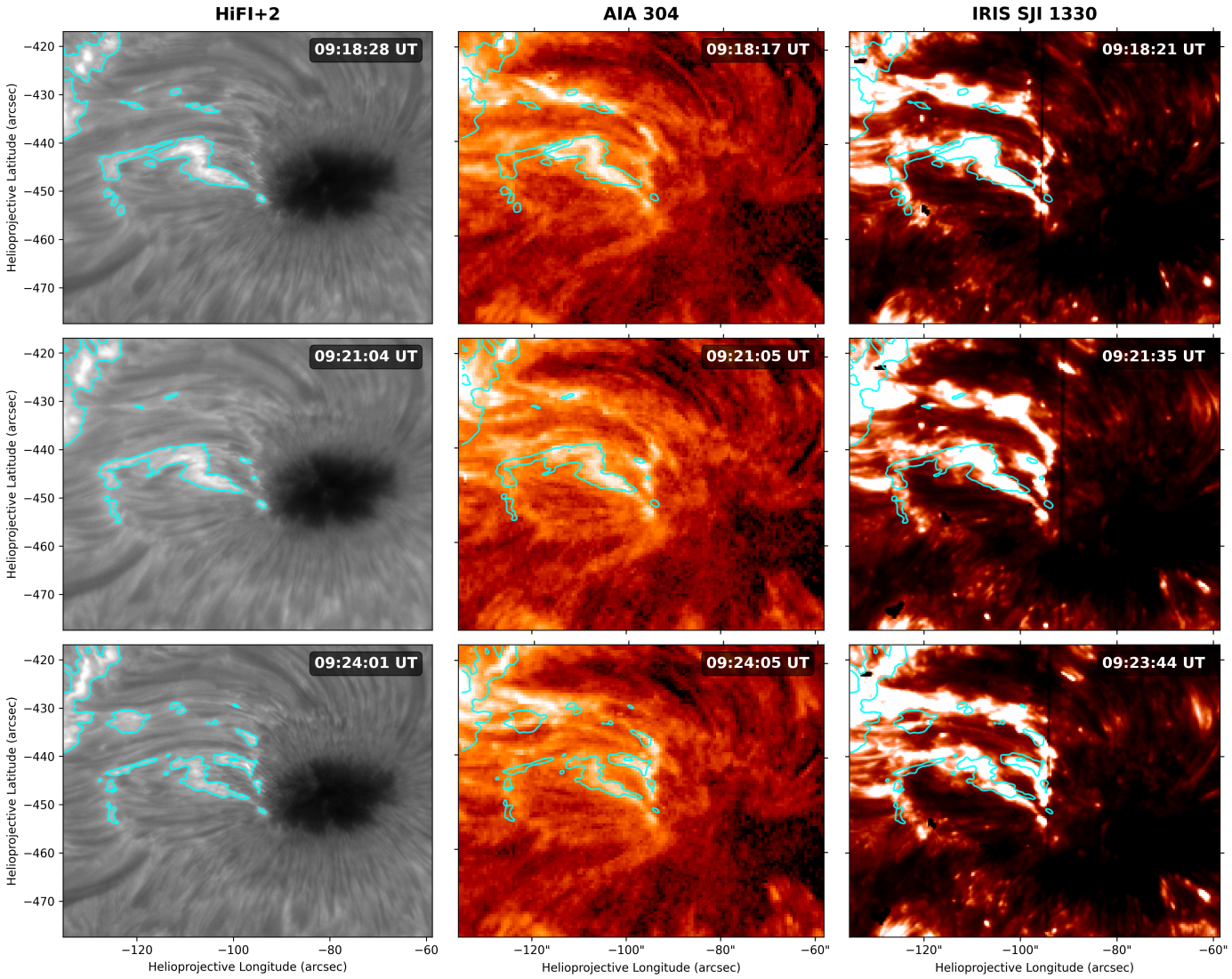


Fig. 5. Temporal evolution of a simultaneous brightening event observed with GREGOR/HiFI (Hα), SDO/AIA 304 Å, and IRIS SJI 1330 Å at three representative times between 09:18 and 09:24 UT. Cyan contours outline the brightest regions identified in the HiFI+2 data.

thus adopted as the preferred setup. This formulation allows the model to account for two distinct physical components along the same line of sight, where the primary slab captures the high-velocity flows while still properly reproducing the underlying photospheric contribution and telluric absorption. In Fig. A.1, we show a comparison between the two-slab and single-slab fits for a representative pixel within the strongly broadened regions. In this case, the presence of two distinct components is evident, and the two-slab model provides a significantly improved fit quality. For He I, the inversion was performed in three successive cycles. In the first cycle, only the parameters Δv, τ, and $v_{\rm LOS}$ were varied to fit the intensity profile, while the magnetic field components (B_x, B_y, and B_z) were kept fixed. This step was typically sufficient to obtain a reliable estimate of the thermodynamic and kinematic properties of the atmosphere. In the second cycle, only the magnetic field components were allowed to vary in order to fit the polarization signals, using the results of the previous cycle as the initial guess. Finally, in the third cycle, all parameters were simultaneously varied to refine the solution. Figures 8 and 9 display the maps obtained from these inversions for the atmospheric parameters in the photosphere and chromosphere, respectively.

For the photosphere (Fig. 8), we show maps of temperature (top), longitudinal magnetic field B_z (middle), and LOS velocity (bottom) at $\log\tau = -1.5$. This depth was selected as it represents a layer where the Si I 1082.7 nm line maintains significant sensitivity across its profile, as shown by the response function analysis in Felipe et al. (2016), and where our inversion results exhibited a smoother spatial distribution. These quantities were retrieved from the inversion of the Si I line using the SIR module integrated within the HAZEL code.

The temperature map at $\log\tau = -1.5$ reveals a structure that is broadly consistent with the intensity distribution shown in Fig. 6. The umbra appears significantly cooler than the surrounding quiet Sun, while the penumbra exhibits intermediate temperature values. Notably, the bright features visible in the intensity map correspond to localized temperature enhancements. A quantitative comparison shows that these regions, outlined by cyan contours in the top panel, exhibit an increase of $\Delta T \approx 260$ K relative to the median QS background. Although the FOV was observed after a C-class flare, the enhanced temperature regions are spatially coincident with areas of high magnetic flux density. This spatial correlation suggests that they might primarily reflect

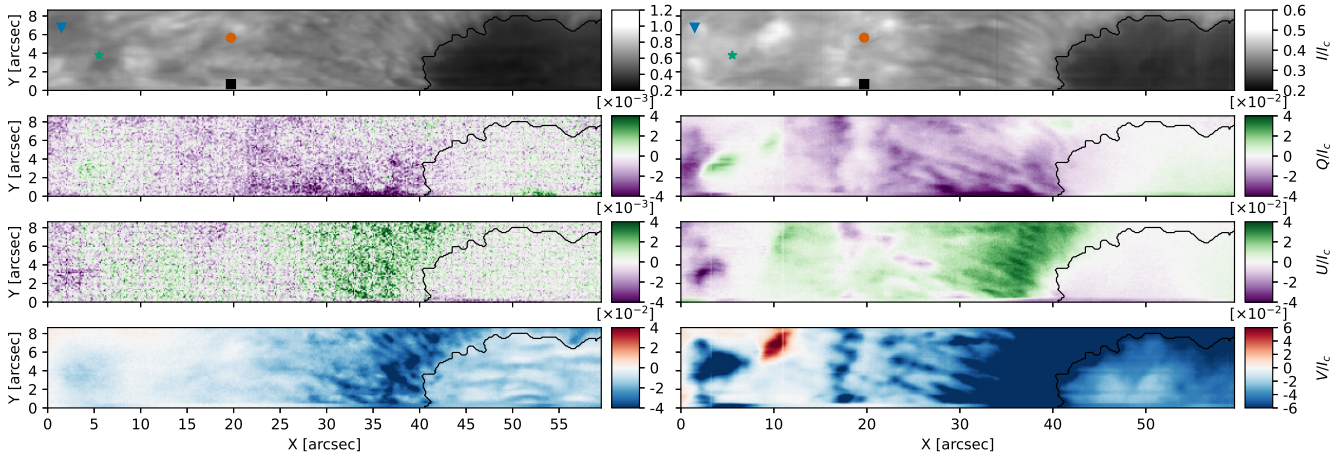


Fig. 6. Maps obtained with GRIS displaying the four Stokes parameters for the red component of the He I triplet (left panels) and the Si I 1082.7 nm line (right panels), both normalized to their continuum intensities. From top to bottom, the panels show I/I_c, Q/I_c, U/I_c, and V/I_c. For each line, the Stokes I/I_c map is evaluated at the line core, while the Q/I_c, U/I_c, and V/I_c maps show values measured in the blue wing, chosen to maximize the visibility of polarization signals. The black contours delineate the sunspot umbra. The inverted triangle, star, circle, and square mark four locations where representative profiles with distinct behaviors were extracted; these are shown in Fig. 7.

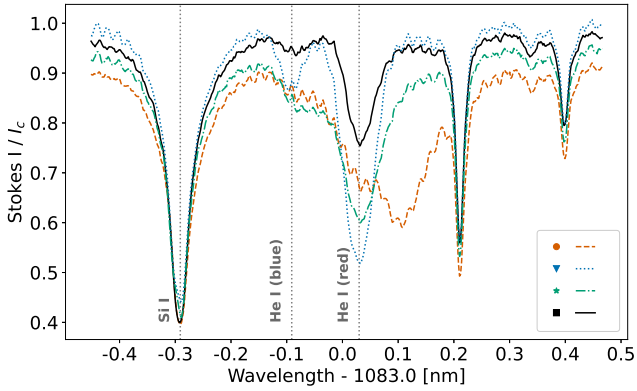


Fig. 7. Stokes I profiles from four representative pixels within the GRIS FOV. The solid line corresponds to a relatively quiet pixel (square in Fig. 6), while the dashed, dotted, and dash-dotted lines correspond to pixels showing distinct spectral features (circle, inverted triangle, and star, respectively). The dashed profile reveals a broadened red component with multiple absorption minima, suggesting the presence of multiple atmospheric components with different velocities. The dotted profile shows strong absorption near 1083.03 nm, while the dash-dotted profile exhibits a very strong and broad absorption feature in a region where also stronger presence of polarization is present.

the signatures of localized magnetic structures, rather than being a direct consequence of the flare heating at photospheric level.

In the B_z map (middle panel), we see that the magnetic field appears smoothly distributed, with filamentary structures in the penumbra and small-scale features in the surrounding quiet Sun. The LOS velocity map (bottom) displays mostly weak flows (up to ±2 km/s), predominantly upflows, interspersed with localized downflow patches. These motions are consistent with standard convective and penumbral flows in the photosphere.

For the chromosphere, we present the results obtained from the inversion (Fig. 9). The two columns show hybrid maps constructed a posteriori by combining the single-slab inversion results with the two-slab configuration, fixed at heights of 3″ and 6″, respectively, only in regions where the profile complexity required the additional component. The left column corresponds to the primary component, `ch1`, which represents the main chromospheric layer and captures the high-velocity flows, while the right column represents the secondary component, `ch2`.

The optical depth maps (top row) show that the sunspot umbra appears nearly transparent, with τ values between 0 and 0.3. This reduced opacity implies a low population of the metastable $1s2s\,^3S$ level, which can be interpreted through two main physical mechanisms. The first hypothesis attributes the depopulation to the absorption of coronal EUV radiation by the cool umbral plume, which inhibits the photoionization-recombination (PR) process (Leenaarts et al. 2016). Alternatively, the reduced electron density in the umbra may alter the competition between PR and collisional excitations, leading to a reduced number of triplet atoms (Andretta & Jones 1997). While the former scenario implies a shielding effect at similar formation heights, the latter suggests that the line forms at different atmospheric depths, which should be reflected in the velocity field.

The optical depth τ exhibits a clear anti-correlation with the intensity map of the red component of the He I triplet (Fig. 6), where darker intensity regions correspond to higher optical depth. This behavior, which is consistent with previous studies indicating stronger He I absorption in regions with enhanced chromospheric density or illumination (Andretta & Jones 1997; Centeno et al. 2009), characterizes the overall structure of the FOV.

The physical nature of these variations is further clarified by an analysis of the relationship between the He I red-component velocities and the optical depth. A statistical check reveals a significant positive correlation between these two parameters outside the umbral region. This behavior suggests a systematic variation of the line formation height in the chromosphere, regulated by local electron density, which provides strong evidence for the PR model (Andretta & Jones 1997).

Within the boundaries delineated by the dashed lines, where the two-slab model was applied, the two components exhibit a distinct separation in their optical depth. Specifically, `ch1` is characterized by significantly higher values of τ compared to `ch2`, with peaks reaching values between 0.9 and 1.0.

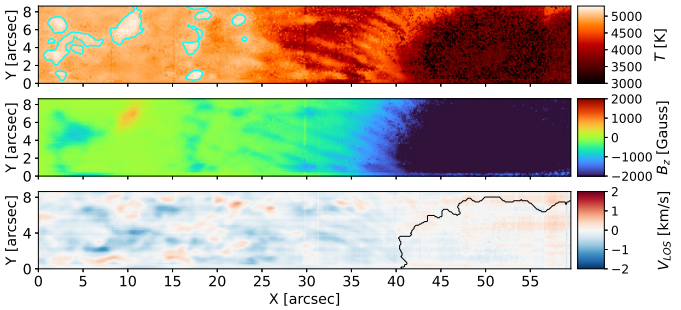


Fig. 8. Photospheric atmospheric parameters retrieved from inversions of the Si I 1082.7 nm line. The panels show maps at $\log \tau = -1.5$ of temperature (top), longitudinal magnetic field B_z (middle), and LOS velocity (bottom). In the top panel, cyan contours identify localized temperature enhancements (corresponding to the 95th percentile of the temperature distribution). In the bottom panel, the black contour delineates the sunspot umbra boundary

The B_z maps (second row of Fig. 9) display the magnetic field signal retrieved from the inversion. In the umbra, B_z reaches up to −1800 G in the first component (`ch1`), indicating a strong longitudinal field. Moving outward from the umbra, the magnetic field strength decreases gradually, although localized enhancements are observed in the region $x \in [0'', 10''], y \in [2'', 6'']$.

The third row displays the LOS velocity $v_{\rm LOS}$. Where a single-slab model is applied, i.e., outside the dashed contours, we observe relatively low velocities that are predominantly positive. In the umbral region, a wave-like pattern of alternating upflows and downflows is visible, suggestive of chromospheric umbral flashes, similar to those reported by Felipe et al. (2025). Within the contoured regions, we find a clear divergence in behavior between `ch1` and `ch2`. In particular, the velocities associated with the primary component reach values of up to ~ 30 km, s^{-1}, indicating strong downflows. These signatures are consistent with chromospheric condensations reported in comparable events, including C-class (e.g., Falchi et al. 2006; Libbrecht et al. 2019) and M-class (Kuckein et al. 2025) flares, as observed in spectral lines such as He I and Ca II.

The bottom row displays the Doppler width Δv. Within the regions where the two-slab model is applied, the two components exhibit distinctly different behaviors. In `ch1`, we observe substantial line broadening, reaching up to ~ 19 km, s^{-1}, which is spatially correlated with the strong downflows. This suggests unresolved velocity gradients or enhanced microturbulence in regions affected by flare-like activity. In contrast, `ch2` shows more uniform and generally lower Doppler widths, consistent with a comparatively more quiescent chromospheric background characterized by weaker dynamical activity.

5. IRIS observations

Figure 5 clearly manifests that the brightening observed with the GREGOR/HiFI+ camera is spatially co-located with emission clearly visible in both the AIA 304 Å and IRIS SJI 1330 Å channels. Building on this multi-instrument connection, this section analyzes the IRIS spectral data acquired during the coordinated campaign. For context, Figure B.1 displays a series of IRIS SJIs taken on 8 August 2023 at approximately 09:18 UT, illustrating the sunspot's surroundings in four passbands. The 1330 Å and 1400 Å passbands predominantly trace the upper chromosphere and transition region, dominated by C II and Si IV line emission, respectively, alongside a UV continuum contribution. Furthermore, the 2796 Å channel samples the chromospheric Mg II k line, while the 2832 Å passband captures the photospheric continuum, thereby probing the deeper atmospheric layers.

In the 1330 Å, 1400 Å, and 2796 Å maps, several bright structures are visible. These brightenings appear particularly concentrated around the sunspot. The 2832 Å image reveals the underlying photospheric structure. Of particular interest is the brightening in the upper-left portion of the FOV, visible in all chromospheric and transition region passbands. To isolate the most intense emission, these brightest regions are highlighted with a blue contour corresponding to the 95th percentile of the IRIS SJI 1330 Å map. This feature coincides with the brightening previously identified in both the SDO/AIA EUV data and the GREGOR observations as shown in Fig. 5, indicating a coherent response of the solar atmosphere across multiple layers during the event.

Figure 10 illustrates the temporal evolution of the brightening event observed in a subFOV of the IRIS SJIs, focusing on the 1330 Å (left panels) and 2796 Å (right panels) passbands. The sequence covers a time interval of approximately twenty minutes, from 09:15 UT to 09:37 UT. The vertical white line marks the position of the IRIS spectrograph slit, which captures a portion of the evolving brightening throughout the sequence. In both channels, a bright structure, elongated along the east-west direction is visible in the left portion of the IRIS FOV, progressively intensifying and evolving over time (highlighted by a blue contour representing the 95th percentile, same as in Fig. B.1). Around 09:28 UT, the emission begins to decrease in brightness, and by 09:36 UT it is almost completely faded in the region crossed by the slit. The 1330 Å channel reveals a particularly enhanced and finely structured emission, with thin, thread-like features. The 2796 Å images display a similar, though slightly less intense, brightening pattern.

Figure B.2 presents the spectroscopic counterpart of the western footpoint of the brightening, showing the temporal evolution of the spectral emission profiles recorded by the IRIS slit as it crossed the region of enhanced emission. The panels display spectra for four diagnostic lines: Si IV 1402.8 Å and C II 1335.7 Å which sample the transition region and middle/upper chromosphere, and Mg II h&k 2796.3 and 2803.5 Å, formed in the chromosphere. Each row corresponds to a spectral line, while the columns show five selected time steps, capturing the rise, peak, and decay phases of the event. The intensity is plotted as a function of wavelength, expressed as $\Delta\lambda$ relative to the line rest wavelength λ_0, with the vertical dashed line indicating the rest position. The region of interest, where the brightening occurs, lies approximately between 60″ and 100″ along the slit.

In the Si IV and C II panels, a clear intensity enhancement is observed at specific positions starting around 09:14 UT and peaking near 09:27 UT. To study the detailed evolution of the spectral profiles, we selected four positions along the slit: Y ≈ 70″ (green), 80″ (blue), 86″ (orange), and a white position located in a very quiet region, included for comparison.

To quantify the plasma motions, the Doppler velocities of the emission lines were derived by applying a Gaussian fit to the observed profiles using the IDL `GAUSSFIT` routine. Starting with Si IV line, the green pixel lies in a region with weak enhancement throughout the sequence. The blue pixel, positioned at the center of the brightening, shows a marked increase in intensity starting at 09:23 UT. The line appears moderately redshifted, with a Doppler velocity of about 25 km s^{-1}, remaining nearly constant over the following three frames, while the intensity shows little

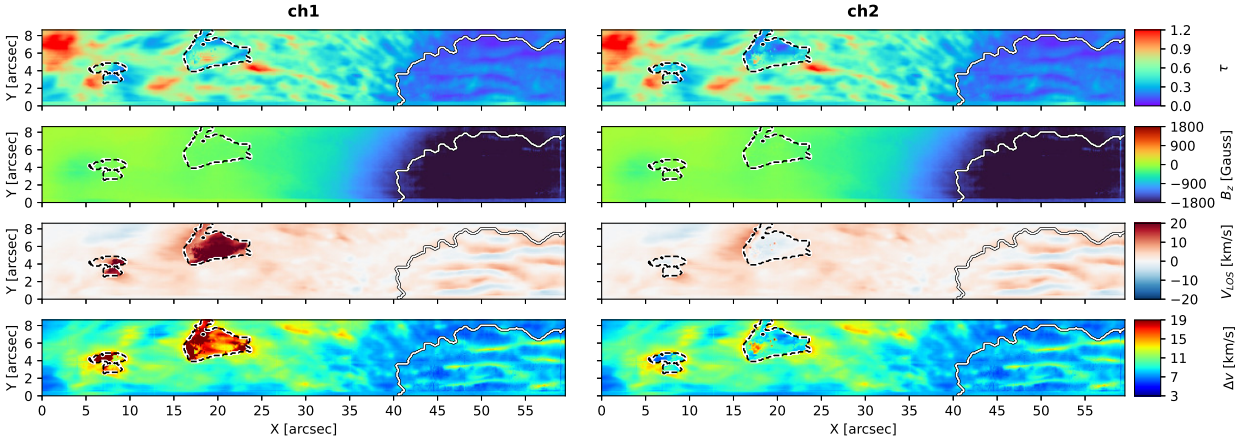


Fig. 9. Maps of the inverted atmospheric parameters. From top to bottom: optical depth τ, line-of-sight magnetic field B_z, line-of-sight velocity $v_{\rm LOS}$, and Doppler width Δv. The solid white/black contours outline the sunspot umbra, while the dashed white/black contours delineate the regions where the two-slab model was applied. Within these dashed boundaries, the left column displays `ch1`, representing the primary component that captures the high-velocity flows, while the right column shows `ch2`, representing the secondary component. Outside these regions, where the complex-profile criterion ($\Delta v > 15$ km s^{-1}) is not satisfied, both columns reduce to the results of the identical single-slab solution.

decrease. The orange pixel displays a sudden increase in intensity at 09:23 UT, followed by an even stronger enhancement at 09:27 UT, before rapidly returning to lower values at 09:32 UT. The line is similarly redshifted at 09:23 UT, with a slight decrease in velocity in the subsequent frames. While the emitting region appears concentrated in the initial frames, it progressively expands across the slit over time.

In the case of the C II line, the second row of panels shows that the brightening appears higher along the slit (increasing Y values) as the event evolves. The green pixel exhibits an early intensity increase at 09:19 UT, followed by a gradual decrease, with the line remaining nearly at rest and showing no significant Doppler shift. The orange pixel, in contrast to its behavior in Si IV, experiences a more gradual intensity rise, reaching a maximum at 09:27 UT and then progressively decreasing. From 09:23 UT onward, a slight redshift of about 10 km s^{-1} is observed. A similar pattern is seen in the blue pixel, which also becomes increasingly asymmetric and stronger in the red wing during the evolution of the event.

Finally, the Mg II k&h lines (third and fourth rows, respectively) show closely matching behavior in both lines. The profiles display marked temporal and spatial evolution, particularly in the orange and blue pixels. Initially, the orange pixel shows a centrally reversed profile, characteristic of optically thick chromospheric conditions. However, around 09:27 UT, the reversal disappears and the line becomes single-peaked, an indication of strong chromospheric heating and a rising source function that fills in the core, likely due to flare-driven energy deposition (Kerr et al. 2015; Rubio da Costa et al. 2016). In contrast, the blue pixel evolves in the opposite direction: starting as a Gaussian-like, single-peaked profile, it returns to a centrally reversed shape at 09:32 UT. This reappearance of the central reversal may indicate a reduced efficiency in chromospheric heating at that time, resulting in a lower source function at line center. Alternatively, it could reflect a partial recovery of the pre-flare atmospheric stratification or the onset of cooling following the heating peak. The green pixel, located outside the main brightening, shows only a modest intensity increase at 09:19 UT, with the line shape remaining largely stable, indicating it was less affected by the dynamic evolution of the flaring event.

6. Discussion

The dynamic response of the chromosphere and transition region to flare heating is typically described within the context of chromospheric evaporation. Theoretical models distinguish between two main regimes based on the magnitude of the incident energy flux (Fisher et al. 1985a,b,c). When the energy flux is below a critical threshold (typically $\sim 10^{10}$ erg cm^{-2} s^{-1}), the process is referred to as "gentle evaporation." In this regime, the chromospheric plasma is heated and expands upward without generating significant downward momentum. This process usually results in blueshifted chromospheric and transition region spectral lines. Conversely, when the energy flux exceeds a threshold of approximately 3×10^{10} erg cm^{-2} s^{-1}, the rapid heating creates a massive overpressure, driving hot plasma upward at velocities of hundreds of km s^{-1} (evaporation) while simultaneously compressing cooler, denser material downward at tens of km s^{-1}. This latter process is known as "chromospheric condensation" or "explosive evaporation." Spectroscopically, explosive evaporation is characterized by blueshifts in hot coronal lines (tracing the upflow) and redshifts in cooler chromospheric and transition region lines (tracing the downflow). Such redshifts have been extensively reported in spectroscopic studies involving lines such as Mg II k, C II, and Si IV (e.g., Tian et al. 2014; Brosius & Daw 2015; Li et al. 2015; Graham & Cauzzi 2015; Kerr et al. 2015; Zhang et al. 2016; Brosius & Inglis 2017; Tian & Chen 2018; Li et al. 2019), as well as in numerical models (e.g., Spadaro et al. 2006).

In our analysis, we observe clear signatures of chromospheric condensation, strongly supporting the explosive evaporation scenario. The analysis of the He I 1083.0 nm spectropolarimetric data from GREGOR/GRIS reveals a localized chromospheric patch with significant dynamical activity. In particular, one spatially confined region shows a highly asymmetric and broadened red component of the He I line profile. A two-component HAZEL inversion was required to reproduce the observed profile, with one of the two components exhibiting strong redshifts (up to 30 km s^{-1}). These velocities are consistent with previous observations of flare-driven chromospheric condensation, where downflows in the range of 20–40 km s^{-1} have been reported in He I during M- and C-class flares (You et al. 1998;

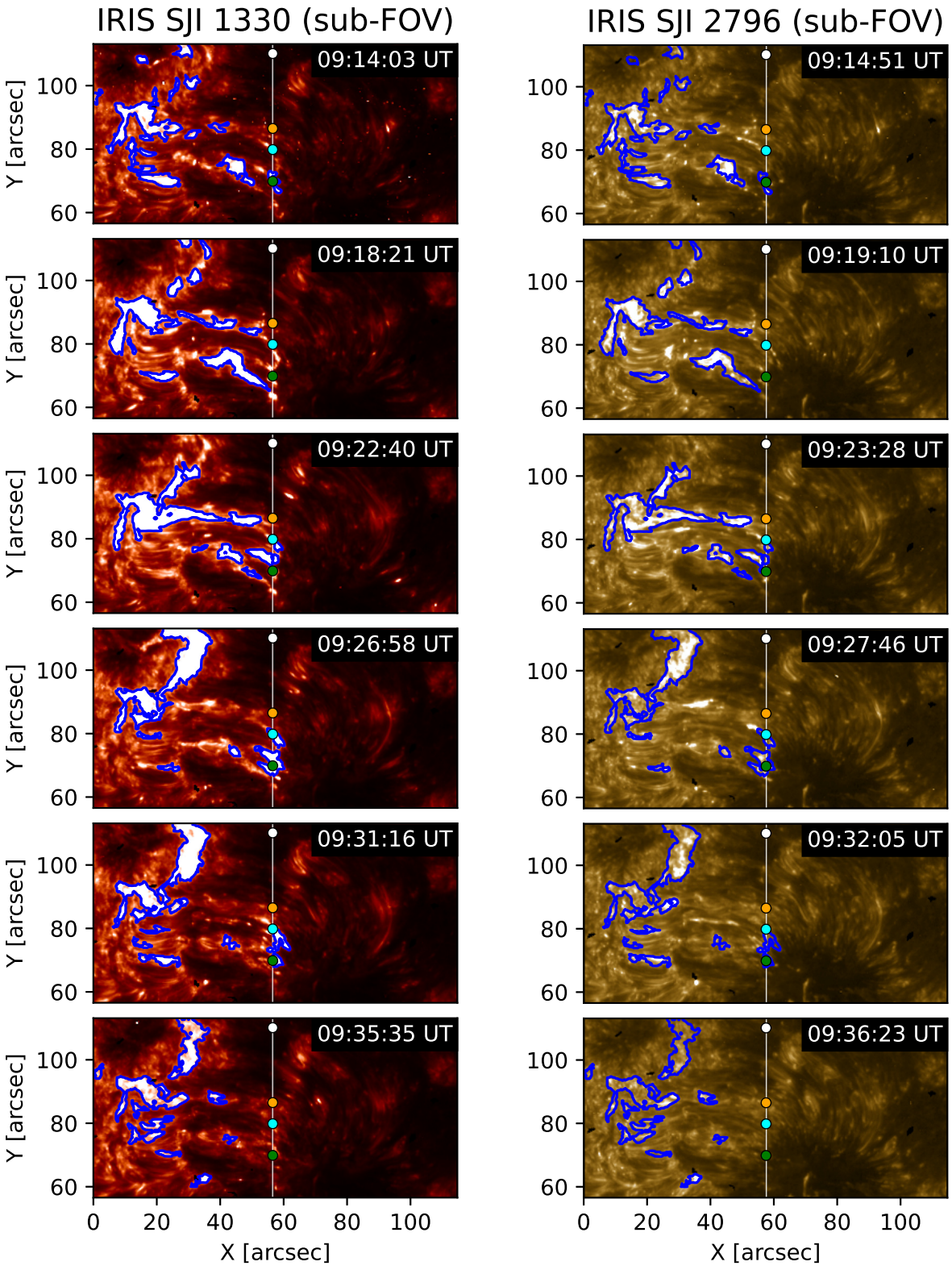


Fig. 10. Temporal evolution of the brightening event as observed in a subFOV of the IRIS SJIs in the 133.0 nm (left panels) and 279.6 nm (right panels) passbands, from 09:15 UT to 09:37 UT. The bright structure evolving in the left part of the FOV is particularly evident in the transition region-sensitive 133.0 nm images, and is also visible in the chromospheric 279.6 nm data. The vertical white line indicates the position of the IRIS spectrograph slit. The three colored dots along the slit indicate the locations where we examine the evolution of the spectra in Fig. B.2. The blue contours represent the 95th intensity percentile derived from the 133.0 nm maps, which are overlaid on both passbands to facilitate spatial comparison.

Kuckein et al. 2025). Our findings suggest that similar dynamical responses are present in this event, with the strong red asymmetry characteristic of downward-moving, rapidly cooling plasma driven by energy deposition from above.

While chromospheric condensation is typically considered a signature of the impulsive phase of flares, previous studies have shown that persistent downflows can occur well into the gradual phase (e.g. Czaykowska et al. 1999; Tian et al. 2015; Tian & Chen 2018). In this context, our detection of strong downflows suggests the occurrence of ongoing localized energy deposition, or prolonged cooling dynamics within the post-flare loops.

The spectral characteristics of the observed lines provide further insight into the physical conditions of the flaring atmosphere. Regarding the He I profiles, the Doppler width retrieved from the HAZEL inversion ($\sim 20\,\mathrm{km\,s^{-1}}$) exceeds the expected thermal broadening at chromospheric temperatures. For $T \sim 1 - 2 \times 10^4$ K (Avrett et al. 1994; Centeno et al. 2008), thermal motions would produce line widths of approximately 5–$10\,\mathrm{km\,s^{-1}}$. The observed excess clearly indicates substantial non-thermal broadening, likely caused by unresolved flow components, steep velocity gradients along the line of sight, or a combination of both, consistent with dynamic, multi-component chromospheric features (Asensio Ramos et al. 2008; Lagg et al. 2007; Sasso et al. 2011). The necessity of a two-component model further supports the presence of complex, stratified flow structures.

Complementary evidence is provided by the IRIS observations. Although the IRIS spectrograph slit does not intersect the exact region of the strong He I redshifts, the slit-jaw images (Fig. B.1) reveal a localized brightening spatially and temporally correlated with the Hα response. The IRIS spectral lines, particularly Si IV and C II (Figure B.2), show redshifted profiles and intensity enhancements in nearby regions, at the flaring footpoint, during the same temporal window as the He I condensation event.

While not strictly cospatial with the redshifted patch observed by GRIS, these signatures suggest that the entire active area experienced the impact of flare energy deposition, resulting in widespread condensation. In particular, the IRIS slit sampled a more peripheral portion of the flare brightening, whereas the redshifted patch identified in the GRIS observations was located approximately 10″ away from the sampled region.

Furthermore, the temporal evolution of the Mg II lines observed by IRIS reveals a clear transition from centrally reversed to single-peaked profiles (Figure B.2). This disappearance of the central reversal has been observed during flares (Kerr et al. 2015; Liu et al. 2015; Panos et al. 2018) and is generally interpreted as a signature of intense chromospheric heating and a rising source function at line center. Reproducing such profiles in simulations typically requires very high electron densities in the line formation region or sharp temperature enhancements in the upper chromosphere (Rubio da Costa et al. 2016; Rubio da Costa & Kleint 2017; Zhu et al. 2019). Additionally, unresolved upflows and downflows within the resolution element can contribute to the formation of single-peaked profiles under non-LTE conditions (Rubio da Costa & Kleint 2017).

While the condensation component (redshifts in cool lines) confirms the impulsive nature of the heating, the corresponding evaporative upflows remain elusive in our dataset. We investigated the high-temperature spectral windows of IRIS, specifically looking for signatures in Fe XII (1349.4 Å, formed at $\sim$ 1.5 MK) and Fe XXI (1354.08 Å, formed at $\sim$ 11 MK). However, no significant emission was detected in these lines. This is likely due to the fact that the flare is not energetic enough to produce an emission measure sufficient to be detected by IRIS, a scenario similar to that reported by Li et al. (2019).

In addition, the absence of evaporation signatures in the hot Fe XXI and Fe XII lines, contrasting with the prominent condensation signatures observed in the cooler lines, may be attributed to that the evaporative flows occurred within a regime where IRIS sensitivity is limited, for example because the temporal integration was too short, or because the IRIS slit did not sample the precise location of these flows. In small-scale events such as this C-class flare, the density of the evaporated plasma might not have reached the threshold necessary for the signal to emerge from the noise floor (Shen et al. 2023).

Furthermore, while the SDO/AIA 131 Å images reveal hot plasma along the flaring loops, this channel has a broad thermal response that integrates emission over a wide range of temperatures. In contrast, IRIS spectral lines have narrow contribution functions. It is therefore possible that the plasma was heated to intermediate temperatures (e.g., 5–8 MK) that contribute to the AIA 131 Å flux but fail to effectively excite the Fe XXI line (which peaks at $\sim$ 11 MK), as discussed by Li et al. (2019).

Finally, the localized and transient nature of evaporation suggests that the spectrograph slit may not have intercepted the footpoint at the exact moment of peak upflow.

7. Summary and conclusions

In this work, we presented a coordinated multi-wavelength analysis focusing on the gradual phases of a small-scale flaring event in AR13394, combining high-resolution spectropolarimetry from GREGOR/GRIS in the He I 1083.0 nm triplet spectral window with UV spectroscopy and imaging from IRIS and high-resolution imaging from GREGOR/HiFI+. Our analysis was focused on studying the atmospheric stratification and thermodynamic response from the chromosphere to the transition region during impulsive energy deposition.

The brightening, first observed by GREGOR/HiFI+ and also identified in IRIS SJIs and AIA filtergrams (see Fig. 5), reveals a coherent response across different atmospheric layers. The analysis of the GREGOR/GRIS observations reveals a localized chromospheric patch characterized by strong dynamical activity. By applying a two-component HAZEL inversion for a selected region, we effectively reproduce these profiles as the superposition of a background atmosphere and a highly dynamic component exhibiting strong redshifts up to $30\,\mathrm{km\,s^{-1}}$. For this downflowing component, the inversion yields a large effective Doppler width of $\sim 20\,\mathrm{km\,s^{-1}}$. Given the complex morphology of the observed profiles, it is not observationally possible to disentangle true microscopic non-thermal broadening from unresolved macroscopic plasma motions. Therefore, we interpret this broad width as the result of unresolved fine-structure flows and strong velocity gradients blended within the resolution element. These kinematic features are consistent with the scenario of chromospheric condensation, tracing dense plasma that is compressed downward by the overpressure generated during the flare impulsive phase.

These signatures of atmospheric condensation are confirmed by the simultaneous IRIS observations. Although the slit did not perfectly align with the He I redshifted patch, the detection of redshifts in transition region lines (Si IV, C II) across the active area suggests a coherent, multi-layer response to the heating event. The ubiquity of these downflows points to an "explosive evaporation" regime, indicating that even in this small-scale event, the energy flux was sufficient to generate overpressure and condensation. Furthermore, the evolution of the Mg II h & k line profiles, which transitioned from a central reversal to a single-peaked morphology, provides evidence of deep heating due to the energy deposition and a rising source function in the lower chromosphere, a behavior that is typical of flare footpoints and

can be related to reduced opacity (e.g., Tian et al. 2014; Li et al. 2015).

The tight cospatiality between the HiFI+2 and IRIS SJI brightenings provides strong evidence for a macroscopic physical connection across different atmospheric heights. Furthermore, the localized redshifted patch within the GRIS scan was observed between 09:20 and 09:24 UT, a temporal window that coincides with the detection of pronounced downflows in the IRIS spectra during the gradual phase. Although the IRIS slit did not intercept the exact location of the GRIS redshifted patch, the simultaneous detection of downflows approximately 10″ away strongly suggests that this dynamic behavior is a widespread process across the flaring region.

Conversely, the peripheral downflows observed by IRIS lack a corresponding kinematic signature in the He I line, as the surrounding regions within the GRIS FOV do not exhibit strong redshifts. This discrepancy may be attributed to several factors, including spatial variations in the atmospheric opacity, or in the specific radiation field required to excite the helium triplet state, highlighting the complex and stratified nature of the energy deposition.

In conclusion, our observations provide a detailed view of the chromospheric response in a small-scale flare, further supporting the established consensus (e.g., Milligan et al. 2006; Brosius 2013; Graham & Cauzzi 2015; Sadykov et al. 2015) that impulsive dynamics such as explosive evaporation are not limited to large eruptive events. However, we find a mismatch between the clearly observed condensation and the elusive evaporation in this event. This fact aligns with findings from other studies (e.g., Brosius & Holman 2010; Li et al. 2019), where the absence of emission or blueshifts in hot lines implies that upward velocities could occur at lower temperatures. This emphasizes the necessity of continuous multi-thermal coverage, combining chromospheric spectropolarimetry with EUV spectroscopy, to fully resolve the mass and energy transport in solar flares.

Looking ahead, the development of the Multi-slit Solar Explorer (MUSE; De Pontieu et al. 2020) and the Solar-C (EUVST) mission (Shimizu et al. 2019) will be pivotal. Unlike current single-slit spectrographs, the MUSE multi-slit design will enable high-cadence spectral imaging of the transition region and corona across a wide field of view, while EUVST will provide seamless and wide coverage of temperature regimes. In this context, these missions will serve as a powerful complement to high-resolution ground-based telescopes focused on chromospheric diagnostics, such as GREGOR and the upgraded IBIS 2.0 instrument to be installed at the THEMIS telescope (Ermolli et al. 2024). Together, these space-based and ground-based facilities will finally enable a comprehensive, multi-layered study of the coupling between atmospheric levels. This synergy will provide the missing link to fully understand the energy release and transport during dynamic solar phenomena, bridging the gap between the evaporation observed in the corona and the condensation in the lower atmosphere.

Acknowledgements. Thanks to the anonymous referee for his/her constructive comments and suggestions, which helped improve the manuscript. The research leading to these results has received funding from the ASI-INAF agreement n. 2022-29-HH.0 for the NASA/MUSE space mission. This research has received financial support from the European Union's Horizon 2020 research and innovation program under grant agreement No. 824135 (SOLARNET). F.F. is grateful to A. Asensio Ramos for his valuable suggestions and to C. Quintero Noda for fruitful discussions. SLG, PR and LC acknowledge support from INAF through Bando per il finanziamento della Ricerca Fondamentale 2023–IDEA-SW project. Support from Italian Space Agency and the Ministry of University and Research under Contract n. 2024-5-E.0 (Space It Up) is gratefully acknowledged. SLG and MM acknowledge support from INAF through Bando per il finanziamento della Ricerca Fondamentale 2023 - Minigrants RSN3. CK acknowledges grant RYC2022-037660-I and SJGM grant RYC2022-037565-I, both funded by MCIN/AEI/10.13039/501100011033 and by "ESF Investing in your future." CK thanks grant PID2024-156066OB-C55, and SJGM grant PID2024-156538NB-I00, both funded by MCIN/AEI/ 10.13039/501100011033 and by "ERDF A way of making Europe." The 1.5-meter GREGOR solar telescope was built by a German consortium under the leadership of the Institute for Solar Physics (KIS) in Freiburg with the Leibniz Institute for Astrophysics Potsdam, the Institute for Astrophysics Göttingen, and the Max Planck Institute for Solar System Research in Göttingen as partners, and with contributions by the Instituto de Astrofísica de Canarias and the Astronomical Institute of the Academy of Sciences of the Czech Republic. The redesign of the GREGOR AO and instrument distribution optics was carried out by KIS whose technical staff is gratefully acknowledged. IRIS is a NASA small explorer mission developed and operated by LMSAL with major contributions to instruments from SAO and the University of Oslo, and with mission operations executed by LMSAL and NASA Ames Research Center.

References

Andretta, V. & Jones, H. P. 1997, ApJ, 489, 375
Andretta, V., Mauas, P. J. D., Falchi, A., & Teriaca, L. 2008, ApJ, 681, 650
Antonucci, E. 1982, Mem. Soc. Astron. Italiana, 53, 495
Antonucci, E., Gabriel, A. H., & Dennis, B. R. 1984, ApJ, 287, 917
Asensio Ramos, A., Trujillo Bueno, J., & Landi Degl'Innocenti, E. 2008, ApJ, 683, 542
Avrett, E. H., Fontenla, J. M., & Loeser, R. 1994, in IAU Symposium, Vol. 154, Infrared Solar Physics, ed. D. M. Rabin, J. T. Jefferies, & C. Lindsey, 35
Aznar Cuadrado, R., Solanki, S. K., & Lagg, A. 2005, in ESA Special Publication, Vol. 596, Chromospheric and Coronal Magnetic Fields, ed. D. E. Innes, A. Lagg, & S. A. Solanki, 49.1
Aznar Cuadrado, R., Solanki, S. K., & Lagg, A. 2007, in Modern solar facilities - advanced solar science, ed. F. Kneer, K. G. Puschmann, & A. D. Wittmann, 173
Beckers, J. M. & Tallant, P. E. 1969, Sol. Phys., 7, 351
Brosius, J. W. 2013, ApJ, 762, 133
Brosius, J. W. & Daw, A. N. 2015, ApJ, 810, 45
Brosius, J. W. & Holman, G. D. 2010, ApJ, 720, 1472
Brosius, J. W. & Inglis, A. R. 2017, ApJ, 848, 39
Centeno, R., Trujillo Bueno, J., Uitenbroek, H., & Collados, M. 2008, ApJ, 677, 742
Centeno, R., Trujillo Bueno, J., Uitenbroek, H., & Collados, M. 2009, in Astronomical Society of the Pacific Conference Series, Vol. 405, Solar Polarization 5: In Honor of Jan Stenflo, ed. S. V. Berdyugina, K. N. Nagendra, & R. Ramelli, 297
Collados, M. 1999, in Astronomical Society of the Pacific Conference Series, Vol. 184, Third Advances in Solar Physics Euroconference: Magnetic Fields and Oscillations, ed. B. Schmieder, A. Hofmann, & J. Staude, 3–22
Collados, M., López, R., Páez, E., et al. 2012, Astronomische Nachrichten, 333, 872
Collados, M. V. 2003, in Society of Photo-Optical Instrumentation Engineers (SPIE) Conference Series, Vol. 4843, Polarimetry in Astronomy, ed. S. Fineschi, 55–65
Czaykowska, A., De Pontieu, B., Alexander, D., & Rank, G. 1999, ApJ, 521, L75
De Pontieu, B., Martínez-Sykora, J., Testa, P., et al. 2020, ApJ, 888, 3
De Pontieu, B., Title, A. M., Lemen, J. R., et al. 2014, Sol. Phys., 289, 2733
Denker, C., Verma, M., Wiśniewska, A., et al. 2023, Journal of Astronomical Telescopes, Instruments, and Systems, 9, 015001
Du, Q.-S. & Li, H. 2008, Chinese J. Astron. Astrophys., 8, 723
Ermolli, I., Cirami, R., Sant, K., et al. 2024, in Society of Photo-Optical Instrumentation Engineers (SPIE) Conference Series, Vol. 13096, Ground-based and Airborne Instrumentation for Astronomy X, ed. J. J. Bryant, K. Motohara, & J. R. D. Vernet, 1309677
Falchi, A., Teriaca, L., & Maltagliati, L. 2006, Sol. Phys., 239, 193
Felipe, T., Collados, M., Khomenko, E., et al. 2016, A&A, 596, A59
Felipe, T., González Manrique, S. J., Martínez-Gómez, D., et al. 2025, A&A, 693, A165
Felipe, T., Khomenko, E., & Collados, M. 2010, ApJ, 719, 357
Fisher, G. H., Canfield, R. C., & McClymont, A. N. 1985a, ApJ, 289, 414
Fisher, G. H., Canfield, R. C., & McClymont, A. N. 1985b, ApJ, 289, 425
Fisher, G. H., Canfield, R. C., & McClymont, A. N. 1985c, ApJ, 289, 434
Gingerich, O., Noyes, R. W., Kalkofen, W., & Cuny, Y. 1971, Sol. Phys., 18, 347
González Manrique, S. J., Kuckein, C., Collados, M., et al. 2018, A&A, 617, A55
González Manrique, S. J., Kuckein, C., Pastor Yabar, A., et al. 2016, Astronomische Nachrichten, 337, 1057
Graham, D. R. & Cauzzi, G. 2015, ApJ, 807, L22

Kerr, G. S., Simões, P. J. A., Qiu, J., & Fletcher, L. 2015, A&A, 582, A50
Kleint, L., Berkefeld, T., Esteves, M., et al. 2020, A&A, 641, A27
Kuckein, C., Collados, M., Asensio Ramos, A., et al. 2025, A&A, 699, A121
Kuckein, C., Denker, C., Verma, M., et al. 2017, in IAU Symposium, Vol. 327, Fine Structure and Dynamics of the Solar Atmosphere, ed. S. Vargas Domínguez, A. G. Kosovichev, P. Antolin, & L. Harra, 20–24
Kuckein, C., González Manrique, S. J., Kleint, L., & Asensio Ramos, A. 2020, A&A, 640, A71
Kuridze, D., Henriques, V., Mathioudakis, M., et al. 2017, ApJ, 846, 9
Lagg, A., Woch, J., Solanki, S. K., & Krupp, N. 2007, A&A, 462, 1147
Leenaarts, J., Golding, T., Carlsson, M., Libbrecht, T., & Joshi, J. 2016, A&A, 594, A104
Lemen, J. R., Title, A. M., Akin, D. J., et al. 2012, Sol. Phys., 275, 17
Li, D., Ning, Z. J., & Zhang, Q. M. 2015, ApJ, 813, 59
Li, H., You, J., Yu, X., & Du, Q. 2007, Sol. Phys., 241, 301
Li, Y., Ding, M. D., Hong, J., Li, H., & Gan, W. Q. 2019, ApJ, 879, 30
Li, Y., Kelly, M., Ding, M. D., et al. 2017, ApJ, 848, 118
Libbrecht, T., de la Cruz Rodríguez, J., Danilovic, S., Leenaarts, J., & Pazira, H. 2019, A&A, 621, A35
Liu, W., Heinzel, P., Kleint, L., & Kašparová, J. 2015, Sol. Phys., 290, 3525
Mauas, P. J. D., Andretta, V., Falchi, A., et al. 2005, ApJ, 619, 604
Milligan, R. O., Gallagher, P. T., Mathioudakis, M., & Keenan, F. P. 2006, ApJ, 642, L169
Panos, B., Kleint, L., Huwyler, C., et al. 2018, ApJ, 861, 62
Penn, M. J. & Kuhn, J. R. 1995, ApJ, 441, L51
Pesnell, W. D., Thompson, B. J., & Chamberlin, P. C. 2012, Sol. Phys., 275, 3
Polito, V., Reep, J. W., Reeves, K. K., et al. 2016, ApJ, 816, 89
Rubio da Costa, F. & Kleint, L. 2017, ApJ, 842, 82
Rubio da Costa, F., Kleint, L., Petrosian, V., Liu, W., & Allred, J. C. 2016, ApJ, 827, 38
Ruiz Cobo, B. & del Toro Iniesta, J. C. 1992, ApJ, 398, 375
Sadykov, V. M., Vargas Dominguez, S., Kosovichev, A. G., et al. 2015, ApJ, 805, 167
Sasso, C., Lagg, A., & Solanki, S. K. 2011, A&A, 526, A42
Sasso, C., Lagg, A., & Solanki, S. K. 2014, A&A, 561, A98
Scherrer, P. H., Schou, J., Bush, R. I., et al. 2012, Sol. Phys., 275, 207
Schmidt, W., Muglach, K., & Knölker, M. 2000, ApJ, 544, 567
Schmidt, W., von der Lühe, O., Volkmer, R., et al. 2012, in Astronomical Society of the Pacific Conference Series, Vol. 463, Second ATST-EAST Meeting: Magnetic Fields from the Photosphere to the Corona., ed. T. R. Rimmele, A. Tritschler, F. Wöger, M. Collados Vera, H. Socas-Navarro, R. Schlichenmaier, M. Carlsson, T. Berger, A. Cadavid, P. R. Gilbert, P. R. Goode, & M. Knölker, 365
Shen, C., Polito, V., Reeves, K. K., et al. 2023, Frontiers in Astronomy and Space Sciences, 10, 19
Shimizu, T., Imada, S., Kawate, T., et al. 2019, in Society of Photo-Optical Instrumentation Engineers (SPIE) Conference Series, Vol. 11118, UV, X-Ray, and Gamma-Ray Space Instrumentation for Astronomy XXI, ed. O. H. Siegmund, 1111807
Spadaro, D., Lanza, A. F., Karpen, J. T., & Antiochos, S. K. 2006, ApJ, 642, 579
Tei, A., Sakaue, T., Okamoto, T. J., et al. 2018, PASJ, 70, 100
Tian, H. & Chen, N.-H. 2018, ApJ, 856, 34
Tian, H., Li, G., Reeves, K. K., et al. 2014, ApJ, 797, L14
Tian, H., Young, P. R., Reeves, K. K., et al. 2015, ApJ, 811, 139
Van Noort, M., Rouppe Van Der Voort, L., & Löfdahl, M. G. 2005, Sol. Phys., 228, 191
Wöger, F. & von der Lühe, II, O. 2008, in Society of Photo-Optical Instrumentation Engineers (SPIE) Conference Series, Vol. 7019, Advanced Software and Control for Astronomy II, ed. A. Bridger & N. M. Radziwill, 70191E
Yadav, R., de la Cruz Rodríguez, J., Díaz Baso, C. J., et al. 2019, A&A, 632, A112
Yadav, R., Díaz Baso, C. J., de la Cruz Rodríguez, J., Calvo, F., & Morosin, R. 2021, A&A, 649, A106
You, J., Wang, C., Fan, Z., & Li, H. 1998, Sol. Phys., 182, 431
You, J. Q. & Oertel, G. K. 1992, ApJ, 389, L33
Zeng, Z., Qiu, J., Cao, W., & Judge, P. G. 2014, ApJ, 793, 87
Zhang, Q. M., Li, D., Ning, Z. J., et al. 2016, ApJ, 827, 27
Zhu, Y., Kowalski, A. F., Tian, H., et al. 2019, ApJ, 879, 19

Appendix A: Comparison between single-slab and two-slab model fits

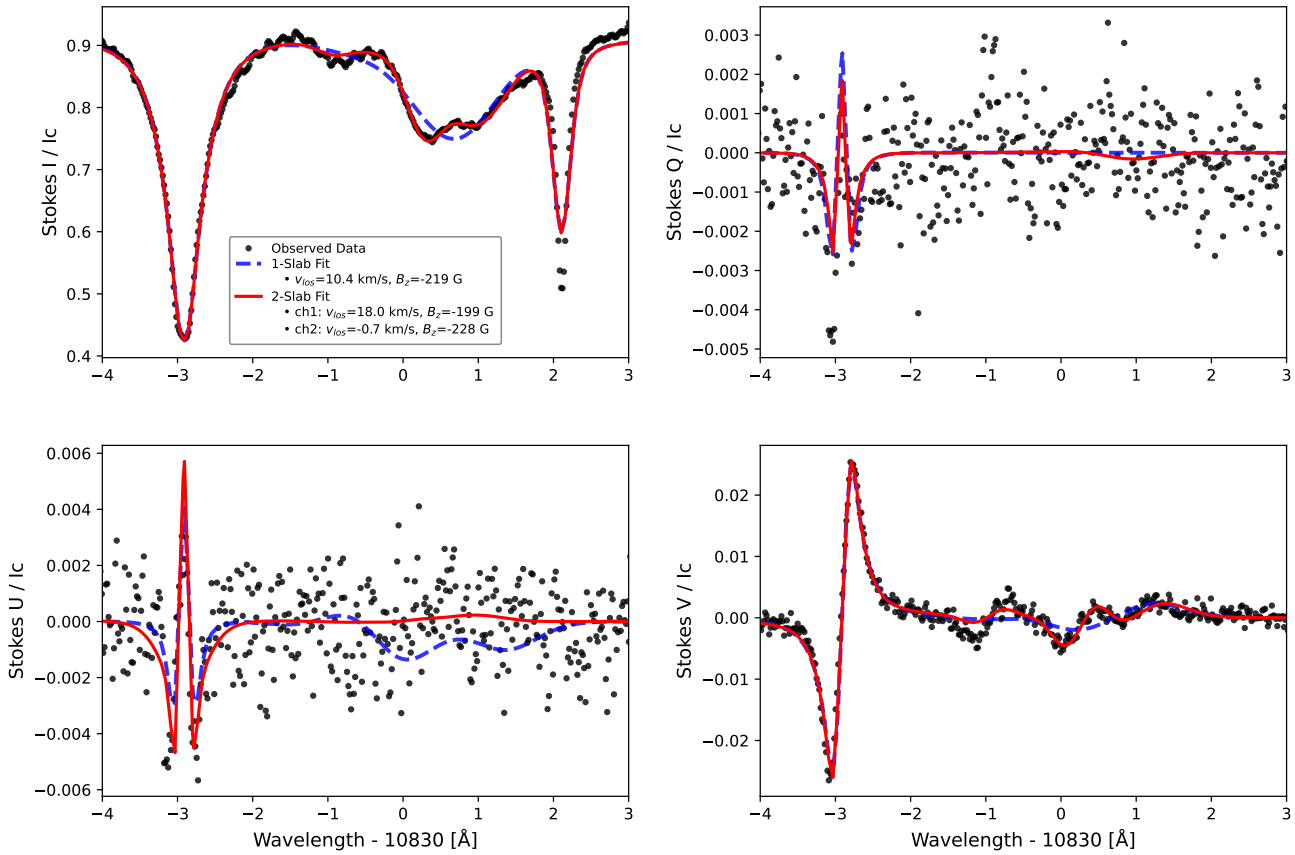


Fig. A.1. Comparison of the He I triplet Stokes profiles (I, Q, U, V) for a representative pixel located within the highly broadened region, where $\Delta v > 15$ km s^{-1}. The observed data (black dots) are compared against the results of the single-slab inversion (dashed blue line) and the two-slab model (solid red line). The inferred v_{LOS} and B_z for both models are reported directly in the legend of the Stokes I panel. As shown, the single-slab model fails to reproduce the pronounced asymmetry in the red wing of the triplet, while the two-slab model successfully captures the secondary high-velocity component, significantly improving the overall fitting quality.

Appendix B: IRIS imaging and spectroscopy

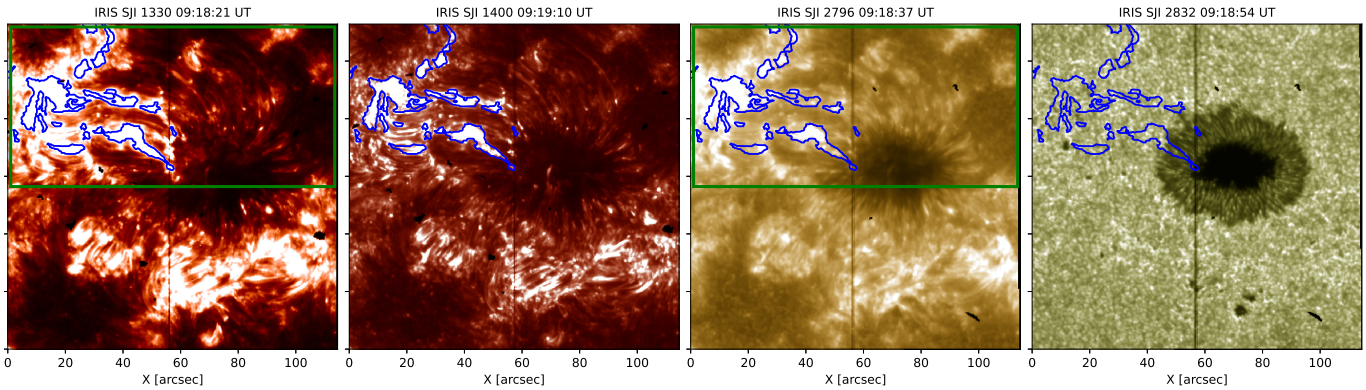


Fig. B.1. Maps derived from IRIS SJI images acquired on 2023 August 8 at around 09:18 UT, showing the field of view recorded at four wavelengths: SJI 1330 Å (first panel), SJI 1400 Å (second panel), SJI 2796 Å (third panel), and SJI 2832 Å (fourth panel). The green box indicates the sub-FOV analyzed in Fig. 10. Blue contours outline the brightest regions in the IRIS SJI 1330 Å data, defined using the 95th intensity percentile.

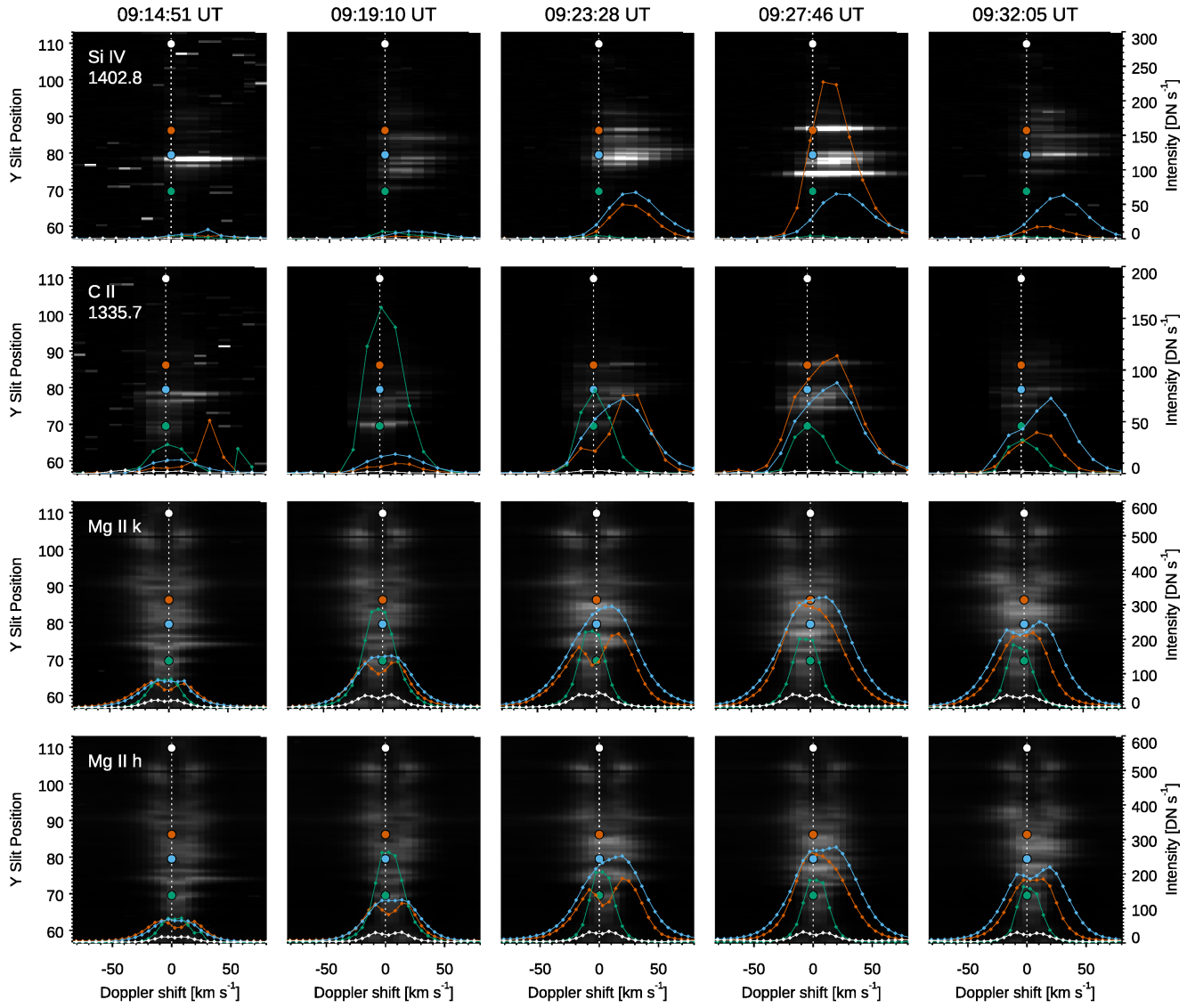


Fig. B.2. IRIS spectra showing the temporal evolution of profiles relevant to the western footpoint of the brightening event in four spectral lines: Si IV 1402.8 Å C II 1335.7 Å Mg II k, and Mg II h. Each panel displays the spectral profiles as a function of Doppler shift and slit position for five selected times. The brightening, located between 60″ and 100″ along the slit, appears as enhanced emission and broadened profiles, particularly in Si IV and C II during the event peak. The colored circles mark the pixels used to extract the spectral profiles shown below each panel, with solid lines. The vertical dashed line indicates the reference wavelength (zero Doppler shift).